Supplementary Information (SI) for Materials Horizons.
This journal is © The Royal Society of Chemistry 2025

Supporting Information (SI)

Hot carrier diffusion-assisted ideal carrier multiplication in monolayer $MoSe_2$

Joonsoo Kim[1,†], Hong-Guk Min[2,†], Sehwan Park[1,†], Jin Cheol Park[1], Junhyeok Bang[3,*], Youngkuk Kim[2,*], and Ji-Hee Kim[4,*]

[1]Department of Energy Science, Sungkyunkwan University

[2]Department of Physics, Sungkyunkwan University

[3]Department of Physics, Chungbuk National University, Cheongju 28644, Republic of Korea

[4]Department of Physics, Pusan National University, Busan 46241, Republic of Korea

[†]These authors contributed equally to this work.

[*]Corresponding author: kimjihee@pusan.ac.kr (J.-H.K.), youngkuk@skku.edu (Y.K.), jbang@cbnu.ac.kr (J.B.)

Note 1. Carrier dynamics in $MoSe_2$

The carrier dynamics of $MoSe_2$ was evaluated by multiple exponential fitting,

$$\Delta A\,(t) = \sum_{i=1}^{n} A_i\ \exp(-t/\tau_i),$$

where A_i represents the amplitude of the exponential component, and τ_i denotes its corresponding decay time.

Monolayer $MoSe_2$ exhibits three distinct decay components both above and below the CM threshold, measured under a consistent photon density of 1.3x10^{12} *photons*/cm^2 (see **Figure S5a** and **Table S1**). These components correspond to: exciton formation time from electron-hole pairs (τ_{fast})[1-5], defect capturing (τ_{defect})[6], exciton recombination process ($\tau_{exciton}$)[4].

The exciton formation time, which is associated with longitudinal optical phonon emission from hot electrons or free carrier states[3, 5, 7-9], remains similar across both excitation energies. However, the amplitude of exciton formation above the CM threshold is approximately twice that observed below the threshold, attributed to the generation of twice as many free carriers through CM.

The subsequent decay component, defect trapping, demonstrates consistent amplitudes and timescales across both excitation conditions. This consistency suggests that the number of excitation photons significantly exceeds the defect density[3], saturating the available trapping sites. While the timescales of the slowest decay component ($\tau_{exciton}$) remain comparable regardless of excitation energy, its amplitude is approximately twice as large above the CM threshold, indicating the generation of twice as many excitons in this regime.

The temporal evolution of CM in monolayer $MoSe_2$ was analyzed in **Figure S5b**. The CM factor indicates that the normalizing parameter from below threshold excitation (1.46E_g) to above threshold excitation (2.30E_g) with identical incident photon density (1.3x10^{12} *photons*/cm^2). The CM factor initially reaches 2 under 2.30E_g excitation, however, gradually decreases to 1 owing to twice amplitude of fast recombination (A_{fast}) and exciton relaxation ($A_{exciton}$) over time delay.

	$A_{fast}(10^{-3})$	τ_{fast} (ps)	$A_{defect}(10^{-4})$	τ_{defect} (ps)	$A_{exciton}(10^{-4})$	$\tau_{exciton}$ (ps)
2.30E_g	7.04 ± 2.08	0.33 ± 0.12	4.21 ± 1.80	6.02 ± 5.7	7.40 ± 1.31	144.8 ± 62
2.06E_g	7.57 ±1.83	0.32 ± 0.05	3.15 ± 2.13	6.36 ± 4.0	7.37 ± 1.20	189.7 ± 78
1.94E_g	3.64 ± 1.50	0.29 ± 0.13	3.91 ± 1.28	8.50 ± 5.5	3.84 ± 1.63	144.8 ± 62
1.46E_g	3.30 ± 1.33	0.31± 0.12	3.15 ± 2.67	5.70 ± 3.8	3.76 ± 0.79	173.6 ± 40

Table S1. Carrier decay parameters of monolayer under 1.3x10^{12} *photons*/cm^2 excitation.

Note 2. Evidence of carrier multiplication

When carrier multiplication (CM) occurs, the excess energy above bandgap excites additional electron-hole pairs. This process manifests through three distinctive fingerprints:

(1) Increase of the maximum $|\Delta\mathrm{A}(E)|_{\max}$

The number of excited carriers is linearly proportional to $|\Delta\mathrm{A}(E)|_{\max}$. As depicted in **Figure 1b** and **1c**, the two-fold increase in $|\Delta\mathrm{A}(E)|_{\max}$ above CM threshold energy ($2.30E_g$) indicates a corresponding two-fold increase of excited carriers.

(2) Transient Stark shift

CM occurring within a few picoseconds, leads to a transient local electric field enhancement, resulting in a transient Stark shift. This phenomenon causes linewidth broadening and redshift at early time delays as observed in **Figure S6**. The increased number of carriers arising from CM rapidly undergo Auger recombination, causing the spectral shift to disappear and return to the state without CM. The temporal evolution of the transient Stark shift is shown in **Figure S7**.

(3) Delayed build-up dynamics

Without CM, the excess energy rapidly thermalizes to band-edge states, leading to prompt build-up dynamics. However, when the photon energy exceeds the CM threshold energy, the build-up time is delayed owing to the additional energy relaxation process (red arrow in **Figure 1b**). Notably, the threshold energy of CM in monolayer $MoSe_2$ is exactly twice the bandgap, such that the delayed build-up is observed at $>2E_g$ excitation (**Figure 1b** and **S8** for monolayer and **Figure S11** for bulk).

These three distinct features serve as clear validation of CM.

Note 3. Evaluation of quantum yield

CM efficiency is evaluated through carrier generation rate per photon. Using transient absorption spectroscopy, we monitored the carrier population based on the spatio-temporally resolved ΔA signal. The absorbed photon density (APD) is calculated by pump fluence, absorption (**Figure S3** for monolayer and **Figure S10** for bulk $MoSe_2$), and beam area:

$$APD = \frac{Power(J) \times Absorption \times e}{Area(cm^2) \times Energy\ (eV)},$$

where e is electric charge to convert Joules to electron volts. We used a 75-μm pinhole to calculate the beam area from the post-to-pre-pinhole power ratio. Detailed APD calculations are shown in **Tables S2** and **S3**. The $MoSe_2$ sample was excited with a sufficiently low photon density (10^{11}–10^{14} photons /cm^2) that nonlinear effects, including many-body effects, were negligible (**Fig. 1c, Figures S9** and **S12**). Based on the maximum ΔA_{max} intensity for the A exciton as a function of absorbed photon density at various pump energies, we were able to obtain the linear slope by linear fitting (**Figure 1c** for monolayer and **Figure S12** for bulk). This linear slope implies the rate of carrier generation per photon. The slopes were identical at excitation $< 2E_g$, whereas the slopes became steeper at pump energies $> 2E_g$. Below $2E_g$, CM does not occur, and the average slope corresponds to a quantum yield (QY) of 1, equivalent to one photon generating one electron-hole pair. Twice that slope is QY = 2, wherein one photon creates two electron-hole pairs. Each slope was normalized by the QY = 1, and the results are presented in **Figure 1d** as a function of excitation energy normalized by the bandgap (E_g). The same evaluation method was applied to analyze the results for bulk $MoSe_2$, as illustrated in **Figure 1d** and **Figure S12**.

Note 4. Quantification of CM efficiency

We quantified CM efficiency based on the competition between relaxation and CM. This model is described in detail in Beard *et al*[10]. CM QY can be depicted as:

$$QY = \sum_{j=1}^{m} j \frac{k_{cool} \prod_{i=0}^{j} k_{CM}^{(i-1)}}{\prod_{i=1}^{j} (k_{cool} + k_{CM}^{(i)})},$$

where k_{cool} is the cooling rate, k_{CM} is the carrier multiplication rate, and *m* is rounding down to the nearest integral product of the photon energy over the bandgap. Thus, $m = \lfloor hv/E_g \rfloor$ and $k_{CM}^{0} = 1$. The competition between k_{cool} and k_{CM} is expressed as:

$$k_{CM} = k_{cool} P \left(\frac{hv - hv_{th}}{hv_{th}} \right)^{s},$$

Where *P* is the competition factor between k_{CM} and k_{cool}, and the exponent *s* is set to 2 due to Keldysh treatment[10, 11]. Finally, CM efficiency (η_{CM}) can be defined as:

$$\eta_{CM} = \frac{P}{P+1} \times 100\%.$$

Using QY, we calculate the ratio $R_{CM} = (N_{CM} - N_0)/N_0 \times 100\%$. N_{CM} (N_0) is the number of carriers generated in the energy range from $2E_g$ to $3E_g$ with (without) CM, respectively. As such, we get N_{CM} (N_0) by integrating QY for a corresponding η_{CM} (for η_{CM}=0).

Note 5. Details regarding CM calculations

In this subsection, we explain the details of the CM calculations used in this study, as depicted in **Figure S14**. We describe the situation where an excited first electron in the initial I_1 state in the conduction band jumps to final state F_1 in the same or another conduction band while transferring its energy and momentum to a second electron in the initial I_2 state in the valence band, such that the second carrier jumps to final state F_2, satisfying energy-momentum conservation. We describe the CM probability $\mu(\hbar\omega, I_1)$ as:

$$\mu(\hbar\omega, I_1) = \sum_{m}^{occ} \sum_{n_{F_1}}^{unocc} \int d\boldsymbol{k}_{F_1} \delta(\hbar\omega - E_{n_{I_1}}(\boldsymbol{k}_{I_1}) + E_m(\boldsymbol{k}_{I_1}))\ \xi(\mathrm{I}_1, F_1) \qquad (1)$$

$$\xi(I_1, F_1) = \sum_{n_{F_2}}^{unocc} \sum_{m_{I_2}}^{occ} \int d\boldsymbol{k}_{I_2}\, d\boldsymbol{k}_{F_2} \delta(E_{n_{F_1}} + E_{m_{I_2}} - E_{n_{I_1}} - E_{n_{F_2}}) \delta(\boldsymbol{k}_{F_1} + \boldsymbol{k}_{I_2} - \boldsymbol{k}_{I_1} - \boldsymbol{k}_{F_2}). \qquad (2)$$

Here, m is the band index for the occupied bands, $\boldsymbol{k}_\alpha$ (n_α and m_α) is the lattice momentum (band indices) of the α state ($\alpha = I_1, I_2, F_1,$ and F_2). The delta function $\delta(\hbar\omega - E_{n_{I_1}}(\boldsymbol{k}_{I_1}) + E_m(\boldsymbol{k}_{I_1}))$ in Eq. (1) imposes energy conservation during the optical excitation process for a given photon energy $\hbar\omega$, while the two delta functions in Eq. (2) impose energy-momentum conservation during the CM transitions $I_1 \rightarrow F_1$ and $I_2 \rightarrow F_2$.

To model the experimental conditions, in which a pump laser with a finite full width at half maximum (FWHM) is used, $\delta(\hbar\omega - E_{n_{I_1}}(\boldsymbol{k}_{I_1}) + E_m(\boldsymbol{k}_{I_1}))$ was approximated by the Gaussian function. The FWHM of the Gaussian function was set at 79.49 and 50.61 meV for the monolayer and bulk cases, respectively, following the accuracy of the pump laser used for the corresponding CM experiments. Direct calculation of the triple integrations over the whole momentum space—one in Eq. (1) and two in Eq. (2)—is highly resource-intensive. We thus proposed an alternative approach, which generalizes the scheme introduced by Bang and Kang[12] into higher dimensions.

Computational Methods for the CM efficiency density N(I_1)

To efficiently evaluate the multiple integrals over momentum space, we extended Bang-Kang's approach[12] as follows. First, for a given first carrier's initial state (I_1), we searched for the final state (F_1) by sweeping over the entirety of the unoccupied bands (2nd and 3rd bands, in this specific example) on a momentum grid within the energy window $\left|E_{3_{F_1}} - E_{I_1}\right| > E_g$ or $\left|E_{2_{F_1}} - E_{I_1}\right| > E_g$, as depicted in **Figure S15a**. Here, E_{I_1} is the energy of I_1 state, $E_{2_{F_1}}$ and $E_{3_{F_1}}$ are the respective energies of the F_1 states in the 2nd and 3rd bands, and E_g is the global energy gap. We note that when $\hbar\omega \sim 2E_g$, the energy difference between I_1 and F_1 should be comparable to E_g ($\left|E_{3_{F_1}} - E_{I_1}\right| \sim E_g$ or $\left|E_{2_{F_1}} - E_{I_1}\right| \sim E_g$ in our specific example) to fulfil the energy conservation imposed by the $2E_g$ optical excitation described by $\delta(\hbar\omega - E_{n_{I_1}}(\boldsymbol{k}_{I_1}) + E_m(\boldsymbol{k}_{I_1}))$ (**Figure S15a**). Once we had obtained the list of F_1 states with energy and momentum differences $\Delta_E(I_1, F_1) = E_{3(2)_{F_1}} - E_{I_1}$, $\Delta_k(I_1, F_1) = \boldsymbol{k}_{F_1} - \boldsymbol{k}_{I_1}$, we shifted the valence bands by $-\Delta_{\mathrm{E}}(I_1, F_1)$ and $-\Delta_{\mathrm{k}}(I_1, F_1)$ in energy-momentum space (**Figure S15b**). I_2 and F_2 can be efficiently and simultaneously determined by counting the density of crossing states between the shifted valence and the conduction bands. This scheme is pivotal to avoid the double momentum integration, $\int\int d\boldsymbol{k}_{I_2} d\boldsymbol{k}_{F_2}$, thereby greatly reducing the computational cost. Note that counting the crossing points can be done much more efficiently by first subtracting the shifted valence band energy from the conduction band energy on the momentum grid and obtaining the density of states (DOS) from the subtracted energies. One can then figure out the existence of the crossing point by simply summing the DOS at the zero energy over the conduction bands on the momentum grid. These results require proper normalization by dividing by the square of the number of sampled $\boldsymbol{k}$-points. **Figure S15c** shows example crossing points and corresponding excited carriers at F_1 and F_2. The crossings occur when the energy difference (indicated by the green double arrows) is zero for a given momentum, as marked by the red circles.

Details of CM calculations for monolayer MoSe₂

CM efficiency was calculated from the 20×20×1 uniform $\boldsymbol{k}$-grid in the first Brillouin zone (BZ) of monolayer $MoSe_2$ (**Figure S16d**). We considered optical excitation by $\hbar\omega = 2E_g \sim 3.08$ eV. The FWHM of 79.5 meV was incorporated into our calculations by introducing the Gaussian function. The color gradient in **Figure S16b**. highlights the band crossings obtained by summing the Gaussian functions from different valence bands. Due to energy conservation, it was safe to search for qualified F_1 states within the energy window $-1.3\, E_g < E_{n_{F_1}} - E_{I_1} < -0.91\, E_g$ for this monolayer case. To obtain the zero-energy DOS, which corresponds to the count of the band crossings, from a discretized $\boldsymbol{k}$-point sampling, we used a Gaussian broadening of 100 meV for the energy difference between the pristine conduction and the shifted valence bands. The normalized CM efficiency was then linearly interpolated along the high-symmetry lines $\Gamma - M - K - \Gamma$. The CM efficiency is localized at the K and K' points. Thus, our calculations support that CM can occur near K and K'.

Details of CM calculations for bulk MoSe₂

CM efficiency was calculated from the 20×20×4 uniform $\boldsymbol{k}$-grid in the first BZ of bulk $MoSe_2$ (**Figure S17d**). Optical excitation by $\hbar\omega = 2E_g \sim 2.38$ eV was considered, and Gaussian functions with FWHM of 50.6 meV were used. We used the lower FWHM in the bulk calculations due to the experimental conditions, in which the lower indirect band gap of bulk $MoSe_2$ requires a lower-frequency laser, accompanied by lower FWHM. The Gaussian functions at a given conduction band point were summed over the valence bands highlighted by the color gradient in **Figure S17b**. We searched qualified F_1 states within the energy window $-1.68E_g < E_{n_{F_1}} - E_{I_1} < -0.84E_g$ for this bulk case. To obtain the zero-energy DOS from a discretized $\boldsymbol{k}$-point sampling, we used a Gaussian broadening of 100 meV for the energy difference between the conduction bands and the shifted valence bands. The normalized CM efficiency was then linearly interpolated along the high-symmetry lines $\Gamma - M - K - \Gamma - A - L - H - A$. These calculations yielded a CM efficiency that was nearly zero over the whole BZ. Thus, our calculations indicate that the CM efficiency of bulk $MoSe_2$ is negligible for the tested $2E_g$ optical excitation.

Note 6. Absence of 2Eg CM channels from hot hole carriers in monolayer $MoSe_2$

In this section, we demonstrate that $2E_g$ carrier multiplication (CM) channels are absent for hole carriers in monolayer $MoSe_2$. The analysis focuses on the ideal CM case at an optical frequency of $2E_g$, where E_g is the direct band gap. The corresponding figure (**Figure S18**) shows $2E_g$ optical excitation in the valence bands near the Fermi level, with pristine band structures depicted in black and energy-shifted valence bands in red. The intersections of these shifted bands with the conduction bands, representing potential $2E_g$ excitation channels, are marked in red. Representative holes and electrons are shown as blue and orange circles, respectively.

For a valence band hole to contribute to CM, it must relax to a higher energy state. However, this process is restricted by Pauli blocking: holes created within a gray-shaded 'forbidden zone' cannot contribute to CM because no unoccupied states exist above them by more than E_g. As shown in the figure, all potential $2E_g$ excitation channels fall within this forbidden zone, indicating that no viable excitations are possible.

Thus, for hole-based CM channels to exist at $2E_g$, there must be Bloch states at the boundary of the Pauli-blocked region, which requires $2E_g$ band nesting. Since $2E_g$ band nesting does not occur in the valence band, we conclude that there are no $2E_g$ CM channels originating from holes in monolayer $MoSe_2$.

Note 7. Spatiotemporal carrier dynamics

We analyzed the spatial carrier distribution $\Delta A(x, t)$ via multiple pump location measurements relative to the probe center (**Figure S19a**). The pump-probe distance (*d*) was controlled by moving the pump position in one direction, across a range of -3 μm to 3 μm. The relative distance between the pump and probe was tracked by a CCD camera. The carrier distribution for the distance at a certain time was fitted by the Gaussian function as follows:

$$\Delta A\,(x,t) \approx N(x,t) = N(0,t) * \exp\left[-\frac{(x-x_0)^2}{2*\sigma^2(t)}\right], \tag{1}$$

where N is the carrier population represented by ΔA, x is the distance between the pump and probe, and σ is the Gaussian width (**Figure S19c**). Spatial broadening over time can be described as a function of the relationship between the Gaussian width and the diffusion coefficient (D):

$$D = \frac{\Delta\sigma^2(t)}{2\Delta t} = \frac{\sigma^2(t)-\sigma^2(0)}{2\Delta t}. \tag{2}$$

Owing to the linear relation between D and $\Delta\sigma^2(t)$, D was obtained by linear fitting in **Figure 4b** and **Figure S20**. The diffusion length (L) was calculated by

$$L = \sqrt{\sigma^2(t) - \sigma^2(0)}. \tag{3}$$

Note 8. Carrier diffusion in $MoSe_2$

The initial fast carrier diffusion coefficients in monolayer and bulk $MoSe_2$ are 1.0×10^4 and 0.3×10^4 cm^2/s, respectively (**Figure 3b**). This rapid carrier diffusion contributes to fast hot carrier expansion. After photoexcitation, the carrier temperature reaches thousands of degrees Kelvin due to lower heat capacity of the electrons, and hot carriers expand rapidly with their excess energy converting to high kinetic energy. After this expansion, negative diffusion occurs from 1–10 ps because of the temperature mismatch between the diffusion of hot carriers and excitons, as seen in previous results[8, 13] (**Figure S20**). During this contraction, carrier–phonon coupling induces thermalization of the hot carriers. They rapidly cool down to band-edge states, losing their kinetic energy and forming excitons. However, carrier–phonon coupling leads to lattice heating within 10 ps, resulting in the recovery of diffusion. The exciton diffusion coefficient is 10.4 cm^2/s (**Figure S20**), almost identical to the reported diffusion coefficient (12 ± 3 cm^2/s) for the $MoSe_2$ monolayer[14]. In contrast, the Gaussian width does not increase in bulk $MoSe_2$ after expansion. The many-body effects are negligible in our findings; hence, one possible explanation is that the defect states can restrict exciton diffusion, causing it to gradually reach a steady state over time. This is supported by the carrier dynamics of bulk $MoSe_2$, where recombination mainly occurs within 10 ps and residual or trap-captured excitons survive for up to 1 ns (**Figure S11**). A similar phenomenon has been observed in perovskite[15] and bulk $MoTe_2$[16].

Note 9. Ballistic transport in $MoSe_2$

As described in main manuscript, the ballistic transport was evaluated using power function, $\Delta\sigma^2(t) = Dt^\beta$, where the β is transport exponent that characterizes the nature of carrier transport. The fitting procedure is detailed as follows:

$$\Delta SWD^2(t) = \begin{cases} 0, & t < 0 \\ Dt^\beta, & t > 0 \end{cases}$$

The transport exponent β is initially close to 2 for time scales below 0.7 ps, indicating that carrier spreads via ballistic manner. However, β decreases significantly to around 1 as the time increases, which is characteristic of a general diffusion process. **(Figure S21)**

Note 10. Scalability and stability considerations for practical application

The exceptional carrier multiplication (CM) efficiency of monolayer $MoSe_2$, achieving a quantum yield of 2.0 at $2E_g$ (Figure 1d), holds significant promise for photovoltaic applications[17, 18]. However, practical implementation requires addressing scalability and stability challenges inherent to 2D materials. For instance, scalable synthesis of uniform, high-quality monolayer $MoSe_2$ remains a critical hurdle, as conventional chemical vapor deposition (CVD) processes can introduce grain boundaries and substrate-induced strain during growth or transfer, which degrade optoelectronic performance. Recent advances in wafer-scale growth[19, 20] offer promising pathways for scalable synthesis. In addition, hybrid in-situ growth architectures[21-24] may reduce transfer-related damage and enhance interfacial charge extraction. Long-term stability concerns, including environmental degradation, can be mitigated through advanced encapsulation strategies using hexagonal boron nitride (hBN)[25, 26], which have demonstrated enhanced stability. Post-growth treatments like pulsed laser-assisted sulfurization[22] or hydrogen plasma passivation[27] could be employed to suppress defect states.

Despite these challenges, the unparalleled CM efficiency achieved in CVD-grown $MoSe_2$ under ambient conditions expands the potential for wafer-scale, stable, high-performance optoelectronics. Continued advancements in synthesis, encapsulation, and integration strategies are expected to bridge the gap between laboratory-scale performance and commercial photovoltaic applications, paving the way for next-generation energy-harvesting, quantum optoelectronic, and photonic technologies.

One additional consideration is the behavior of intermediate-layer $MoSe_2$. While our study focuses on monolayer and bulk $MoSe_2$, intermediate (few-layer) systems offer further insight into the role of CM in 2D layered system. Intermediate layers are expected to exhibit a gradual transition in electronic properties, with reduced quantum confinement compared to the monolayer. The recent work on 2D layered black phosphorus revealed a continuous reduction in CM efficiency as the number of layers increases (from 2L to 4L)[28], suggesting a similar trend expected in $MoSe_2$. Moreover, studies have reported that the transition from a direct to an indirect bandgap in $MoSe_2$ emerges as early as the bilayer[29] or trilayer[30], where the emergence of an indirect bandgap suppresses CM by introducing momentum mismatches that limit energy-conserving pathways. These findings further emphasize the superiority of the monolayer form for achieving ideal CM efficiency.

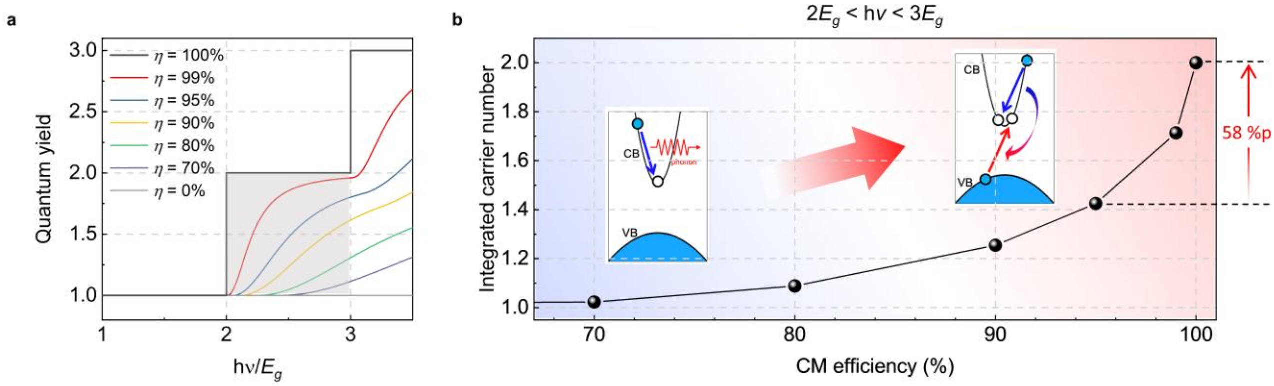

Figure S1. **Carrier multiplication.** Quantum yield as a function of photon energy normalized by the bandgap energy (*hv*/E_g) for various carrier multiplication (CM) efficiencies (η_{CM}). The step-like increase in QY at $hv = 2E_g$ represents the maximum limit of CM, while lower efficiencies result in gradual increases. The shaded region indicates the range used for integrating the number of generated carriers. (b) Correlation between CM efficiency and the integrated number of carriers generated from (a) within the range $2Eg < hv < 3Eg$. Insets illustrate the CM process: at lower efficiency, energy loss channel dominate, reducing carrier generation. At higher efficiency, energy is efficiently utilized to generate multiple carriers through CM. It is worth noting that while CM efficiencies of 95% and 99% are close to the ideal CM, the generated carrier densities are 58% and 29% fewer than those of the ideal, respectively. This discrepancy becomes more pronounced over extending range of photon energies.

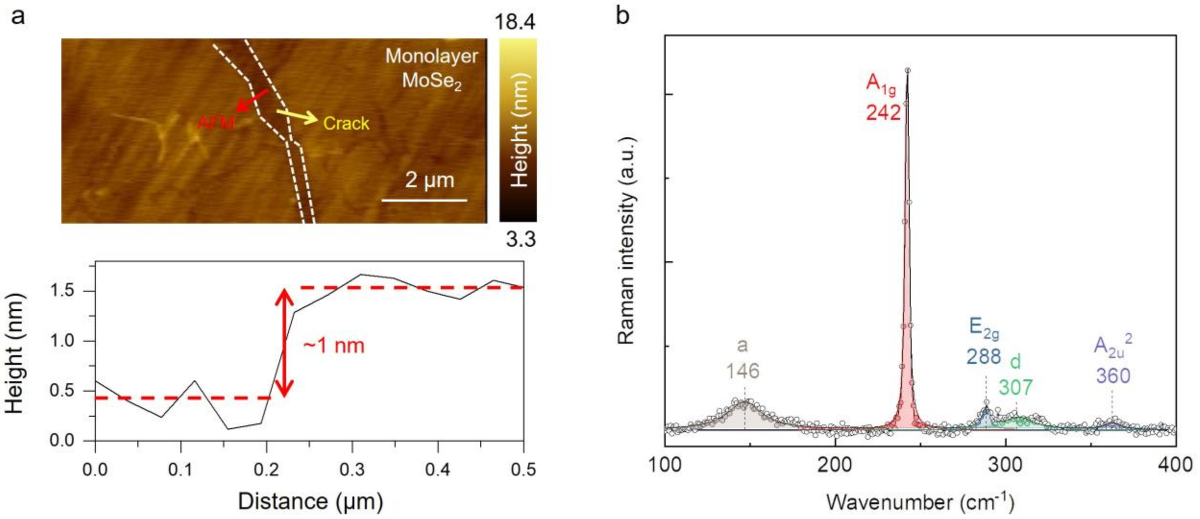

Figure S2. **Sample characterization.** (**a**) Atomic force microscopy (AFM) image (top) and height profile (bottom) of our $MoSe_2$ monolayer. We determined that the thickness of the $MoSe_2$ sample was 1 nm, which is close to typical thickness of a transition metal dichalcogenide (TMD) monolayer[31]. (**b**) Raman spectrum of the $MoSe_2$ monolayer. The spectrum was fitted using a Lorentzian function, showing peak position and vibration mode. The peak positions are identical to those of a $MoSe_2$ monolayer[32].

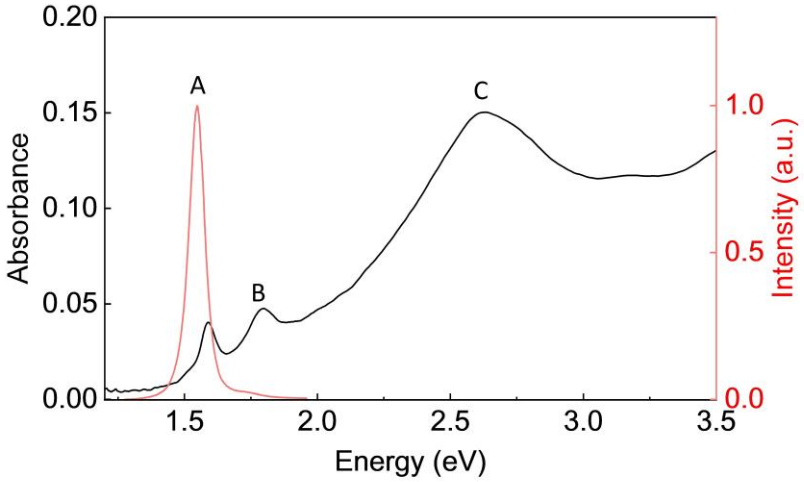

Figure S3. Absorption and photoluminescence spectra of monolayer $MoSe_2$. The absorption spectrum of the monolayer is shown in black, with distinct exciton peaks labeled as A, B, and C excitons. The red curve represents the photoluminescence (PL) spectrum, corresponding to the A exciton peak..

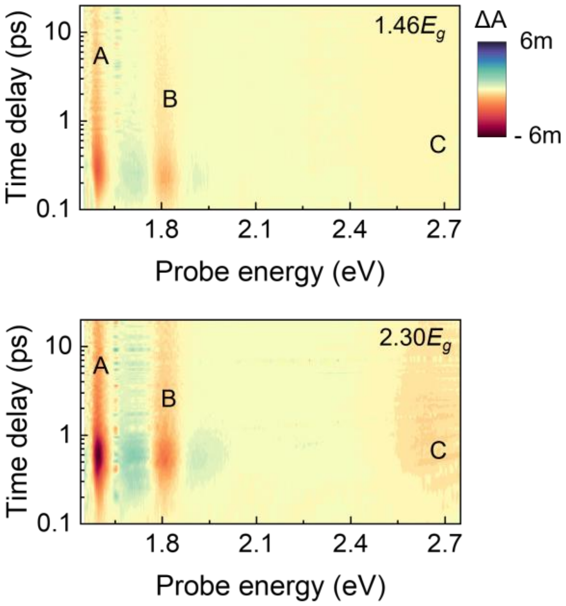

Figure S4. **Transient absorption map of monolayer MoSe₂.** Transient absorption spectroscopy using pump energies of $1.46E_g$ (2.25 eV, **a**) and $2.30E_g$ (3.54 eV, **b**) with the same photon density (1.5×10^{12} cm^{-2}). After excitation, the monolayer exhibits three photobleaching signals (*i.e.*, the A, B, and C excitons), as observed at the absorption spectrum (**Figure S3**). Despite experiencing the same photon density, the intensity of ΔA (*i.e.*, the excited carrier density) is higher at $2.30E_g$ than $1.46E_g$ owing to CM.

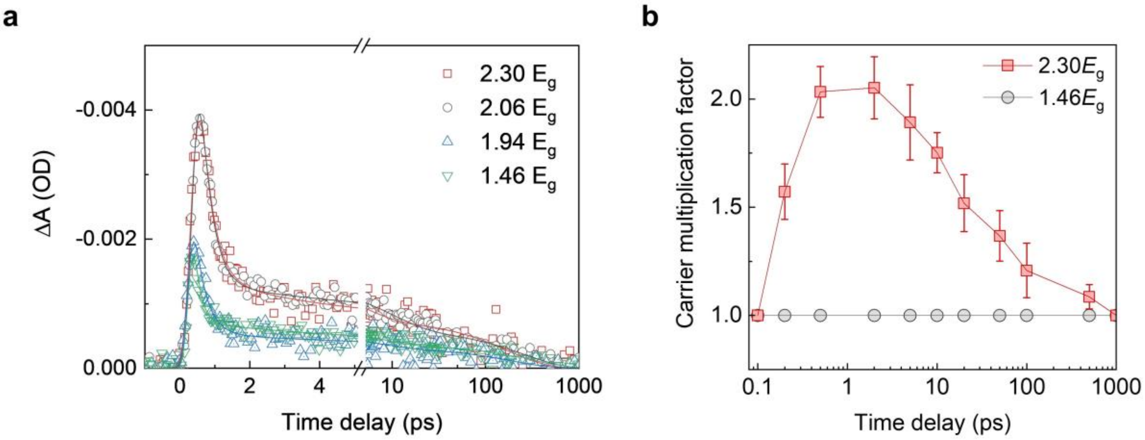

Figure S5. Carrier dynamics of MoSe$_2$. (**a**) Carrier dynamics of monolayer MoSe$_2$ under above CM (2.30E_g, 2.06E_g) and below CM threshold energy (1.94E_g, 1.46E_g) excitations. The transient absorption signal (ΔA) is plotted as a function of time delay, showing two-fold increase in amplitude owing to CM. (**b**) The temporal evolution of Carrier multiplication factor. The factor is obtained by normalizing the 2.30E_g excitation (red squares, **Figure S5a**) to the 1.46E_g reference (gray circles, **Figure S5a**), which is set to factor of 1.

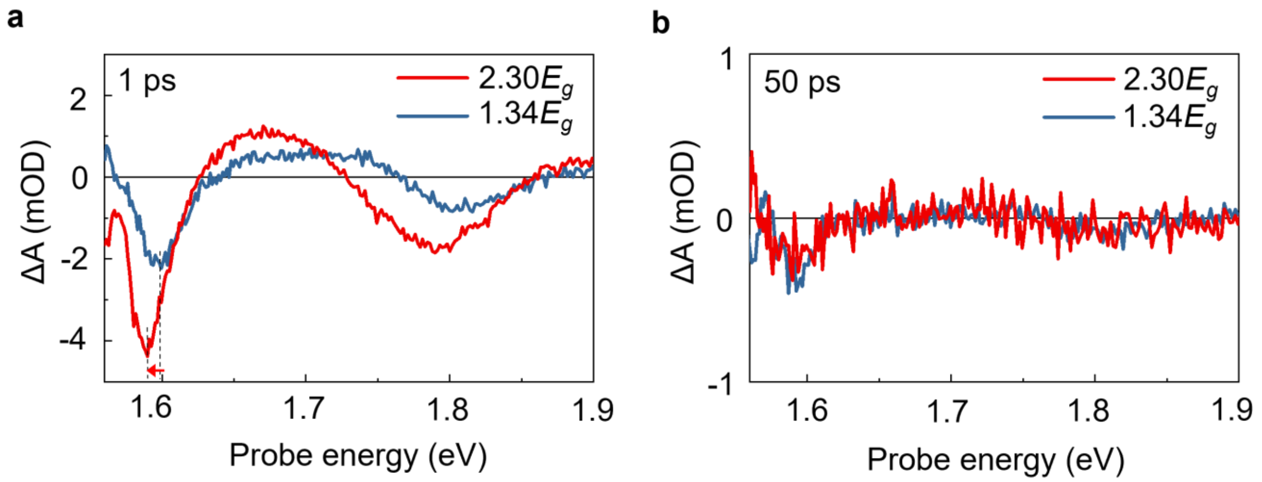

Figure S6. **Transient absorption spectrum of monolayer $MoSe_2$.** Transient absorption spectra were obtained by fixing the time delays to (**a**) 1 ps and (**b**) 50 ps with same photon density (1×10^{12} cm^{-2}). There are two obvious signatures of carrier multiplication. First, the carrier population at $2.30E_g$ excitation is twice as high as that at $1.34E_g$. Second, two PB peaks at $2.30E_g$ are red-shifted at 1 ps (red arrows) due to Stark shift, compared to those at $1.34E_g$. The validation of CM is explained in detail in **Note 2** in **Supporting information**.

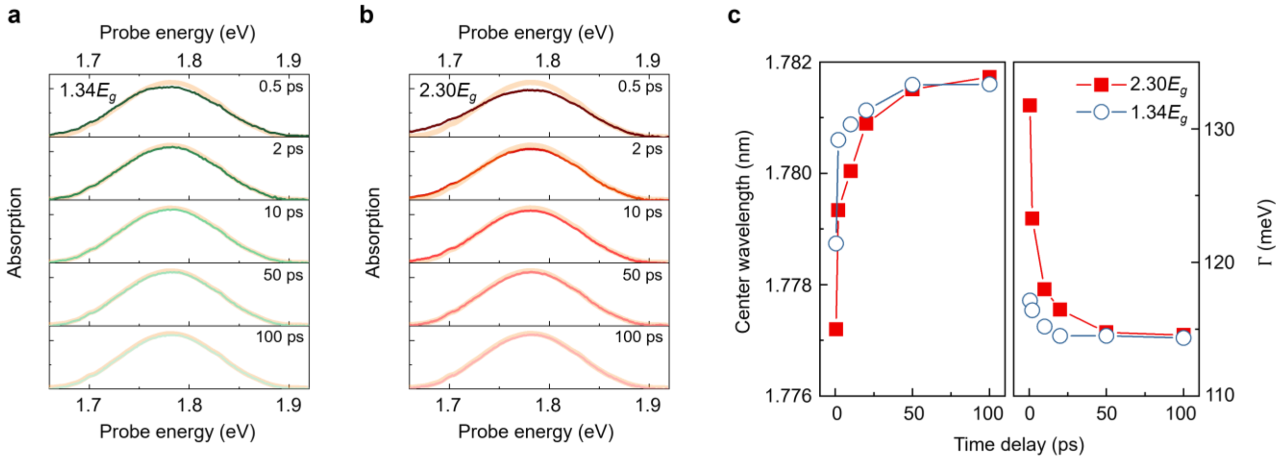

Figure S7. **Transient absorption spectrum shift and broadening.** We investigated transient spectra at 0.5, 2, 10, 50, and 100 ps with pump energies of $1.34E_g$ (**a**) and $2.30E_g$ (**b**). The time evolution of the spectra was fitted to a Gaussian function, and the center wavelengths and linewidth are plotted in (**c**). The temporally longer shift and broadening at $2.30\,E_g$ were induced by local electric field enhancement owing to CM.

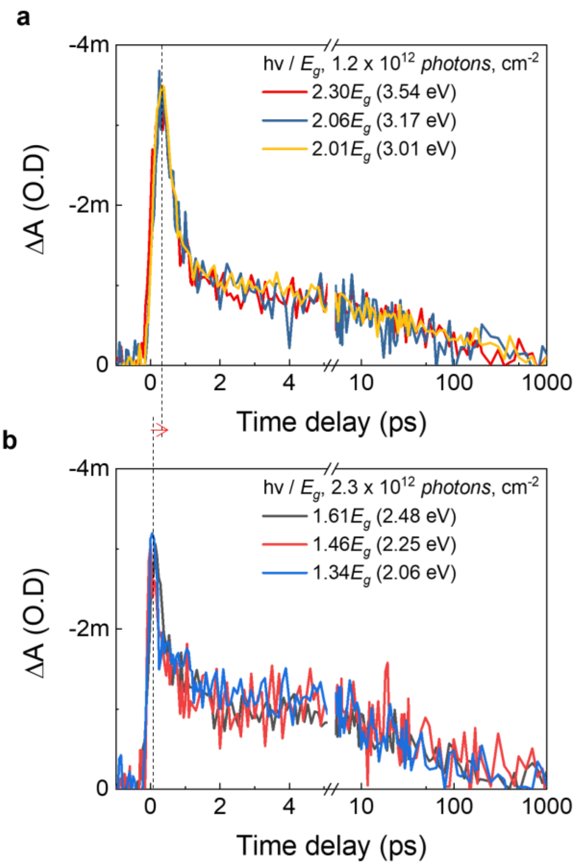

Figure S8. **Carrier dynamics at the A exciton with different excitation energies.** The carrier dynamics were investigated to evaluate CM with photon energies (**a**) above or (**b**) below $2E_g$ at the A exciton state. Considering that ΔA represents photoexcited carrier density, ΔA intensities are equal under the same photon density conditions. However, above $2E_g$, the intensity is observed to be twice that compared to below $2E_g$ owing to CM. Moreover, the rising dynamics above $2E_g$ are slower (red arrow) than those observed at excitation $< 2E_g$, providing evidence of the CM.

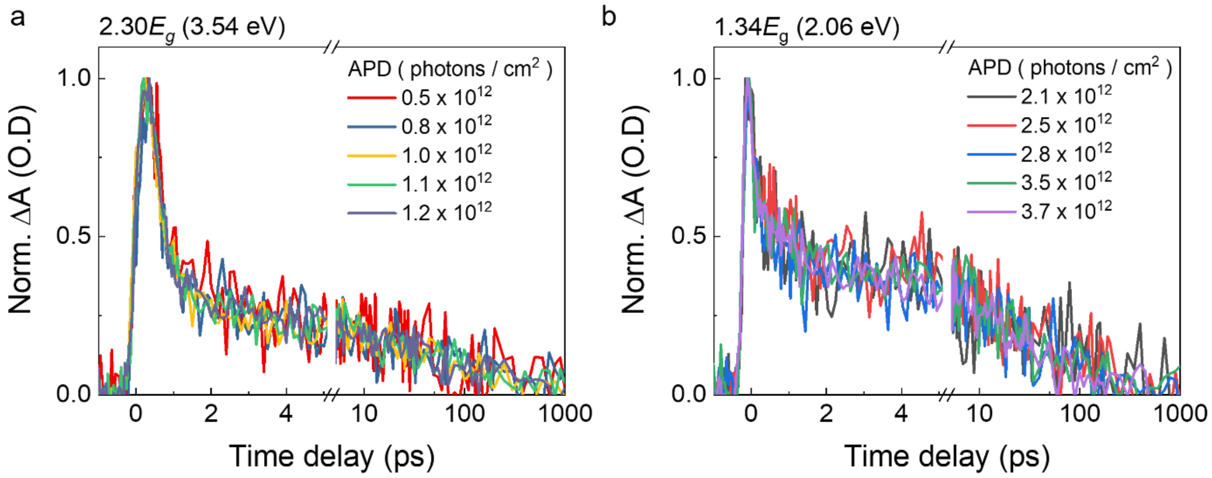

Figure S9. **Normalized carrier dynamics at the A exciton.** The ΔA dynamics were normalized with different photon density and pump energies at the A exciton state. The normalized ΔA dynamics were equal, even though the fluence increased. Moreover, the maximum ΔA intensity was linear as a function of photon density (**Figure 1c**). This indicates that our investigation of CM was performed in a linear regime where non-linear effects are negligible.

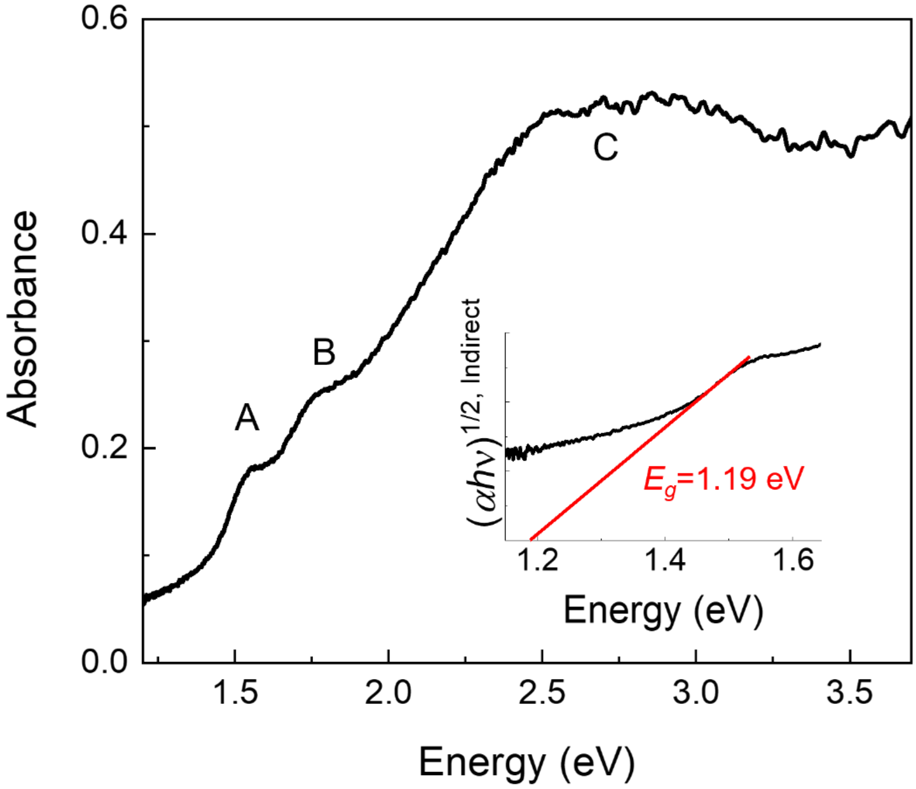

Figure S10. **Optical characterization of bulk $MoSe_2$.** Steady-state absorption of 30-nm bulk $MoSe_2$, including multiple peaks for the A, B, and C excitons. The inset shows a Tauc plot to determine the optical bandgap of bulk $MoSe_2$, revealing an indirect bandgap of 1.19 eV[32, 33].

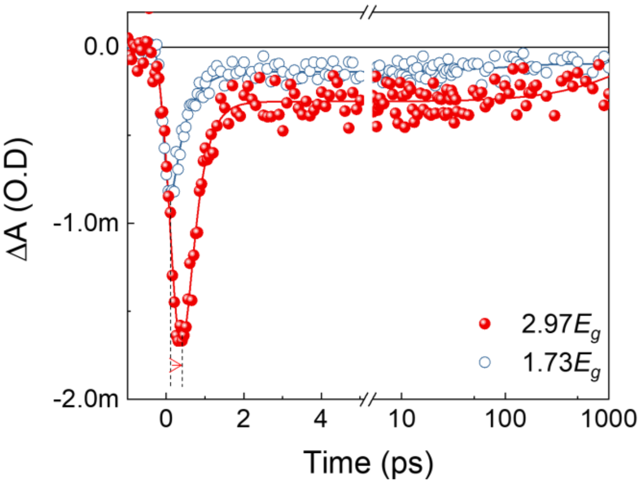

Figure S11. **Transient absorption of bulk MoSe₂.** Transient absorption kinetics with excitation at 2.97E_g (red) and 1.73E_g (blue). The absorbed photon density was fixed at 1 × 10^{14} photons/cm^2.

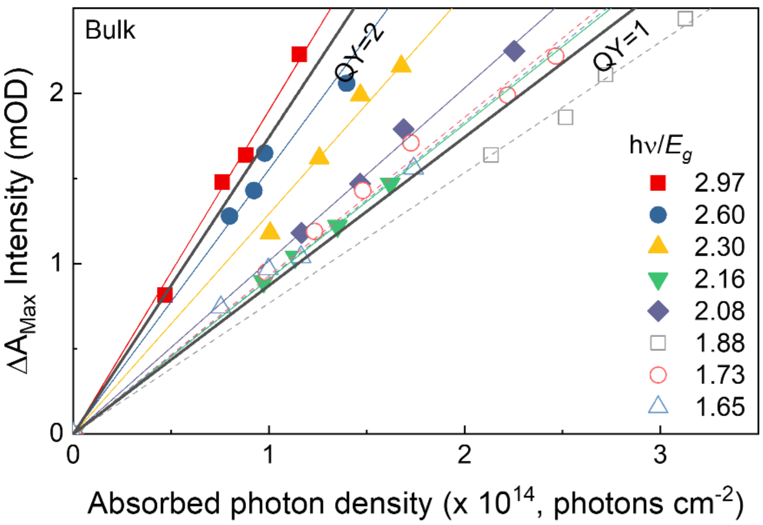

Figure S12. **CM evaluation in bulk $MoSe_2$.** The CM evaluation of bulk was performed in the same procedure as the monolayer in **Figure 1c**.

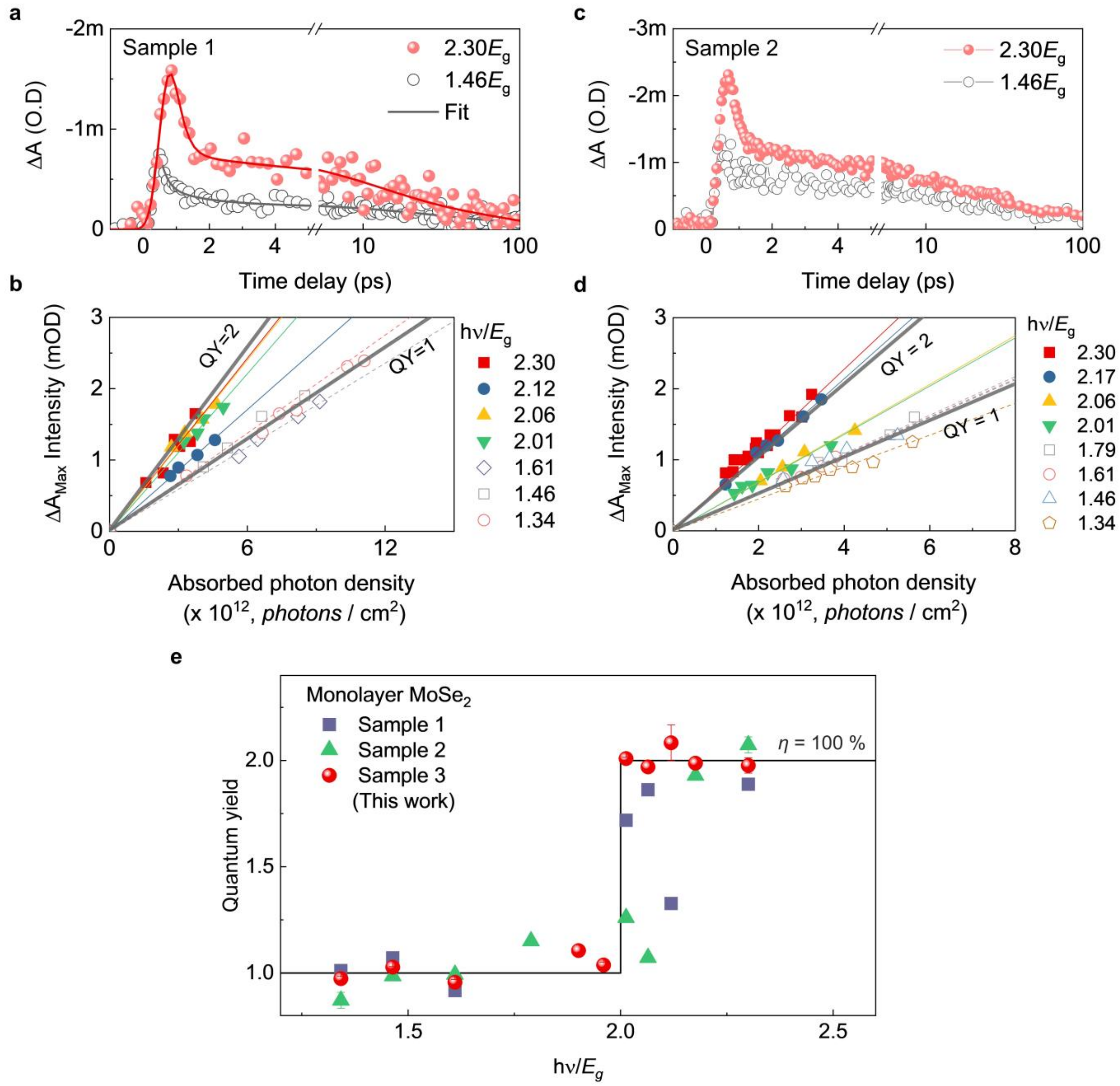

Figure S13. Reproducibility of carrier multiplication in monolayer MoSe$_2$. (**a**, **c**) Time-resolved carrier dynamics at the A exciton under 2.30E$_g$ and 1.46E$_g$ excitation, measured for two samples (Samples 1 and 2, respectively). The absorbed photon density was set to 3.2×10^{12} *photons*/cm^2 in (**a**) and 3.0×10^{12} *photons*/cm^2 in (**c**). (**b**, **d**) The maximum intensity of ΔA as a function of absorbed photon density for various excitation energies from Sample 1 and Sample 2, respectively. (**e**) QY was compared against pump energy, normalized by bandgap (E_g), across Sample 1 (**b**), Sample 2 (**d**) and sample 3 (this work, see **Figure 1d**), highlighting the reproducibility of the CM effect.

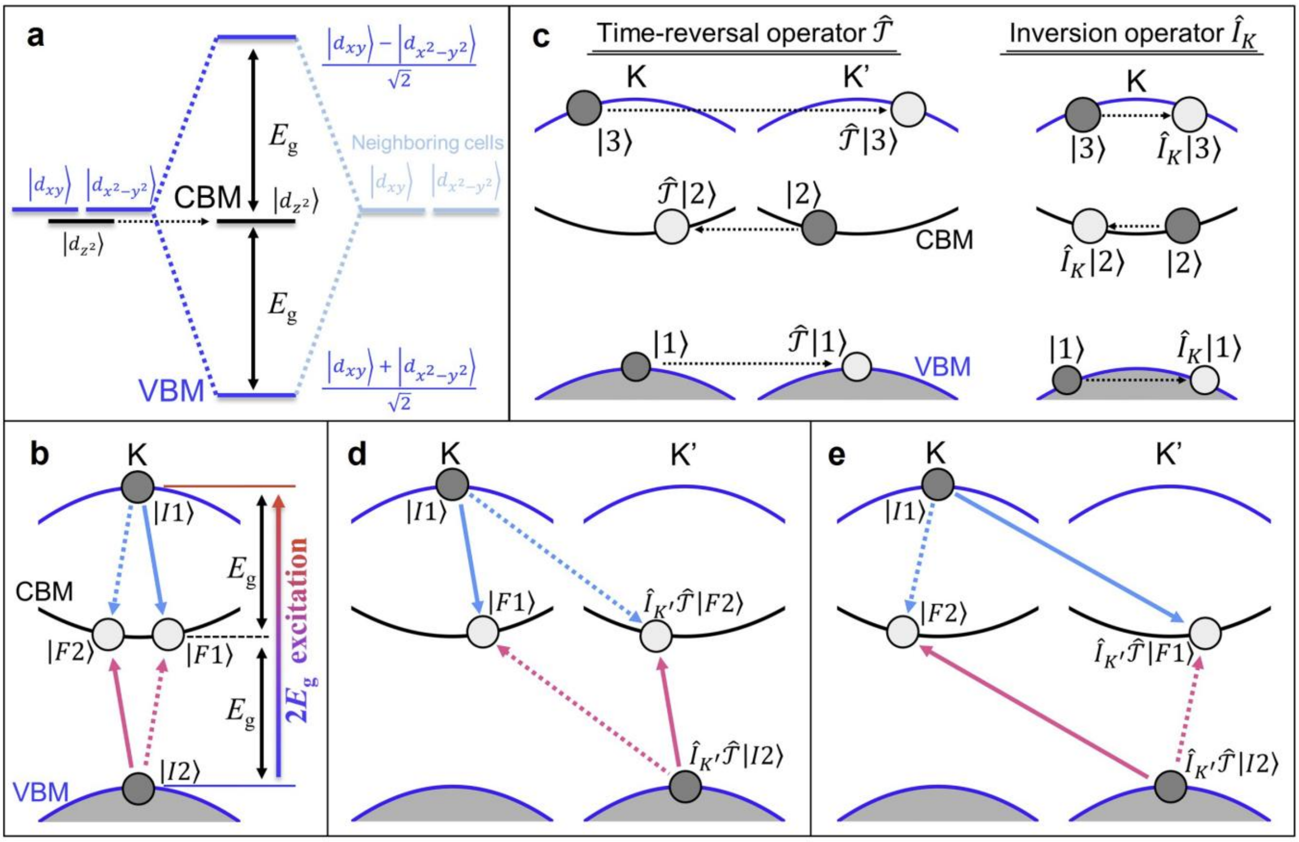

Figure S14. Inter-valley and intra-valley carrier multiplication process due to the valley symmetries. (**a**) Schematic of orbital hybridization shown in the band structure of monolayer $MoSe_2$. For simplicity, we represent the three important orbitals $|d_{z^2}\rangle$, $|d_{x^2-y^2}\rangle$, and $|d_{xy}\rangle$ near the Fermi level in the vicinity of K and K' points. $|d_{x^2-y^2}\rangle$ and $|d_{xy}\rangle$ (in blue) are hybridized through coupling with their counterparts in neighboring cells (in sky blue), forming the bonding and antibonding levels. This positions the $|d_{z^2}\rangle$ level near the middle of the bonding and antibonding levels. **b,** An example of the intra-valley CM channel. **c**, Schematic of the time-reversal operator $\hat{\mathcal{T}}$ and the local inversions operator at K (or equivalently K') $\hat{\mathcal{I}}_{K\,(K')}$. The two blue and one black bands correspond respectively to the bonding, antibonding, and $|d_{z^2}\rangle$ levels in (**a**). (**d**, **e**) Inter-valley CM channels. For the intra-valley CM channel comprising (I_1, I_2, F_1, F_2) in (**c**), one inter-valley CM channel in (**d**) is generated by applying the $\hat{\mathcal{T}}$ and $\hat{\mathcal{I}}_K$ operators to I_2 and F_2. Another inter-valley CM channel in (**e**) is generated by applying these two operators to I_2 and F_1. Solid and dotted arrows represent direct and exchange processes, respectively.

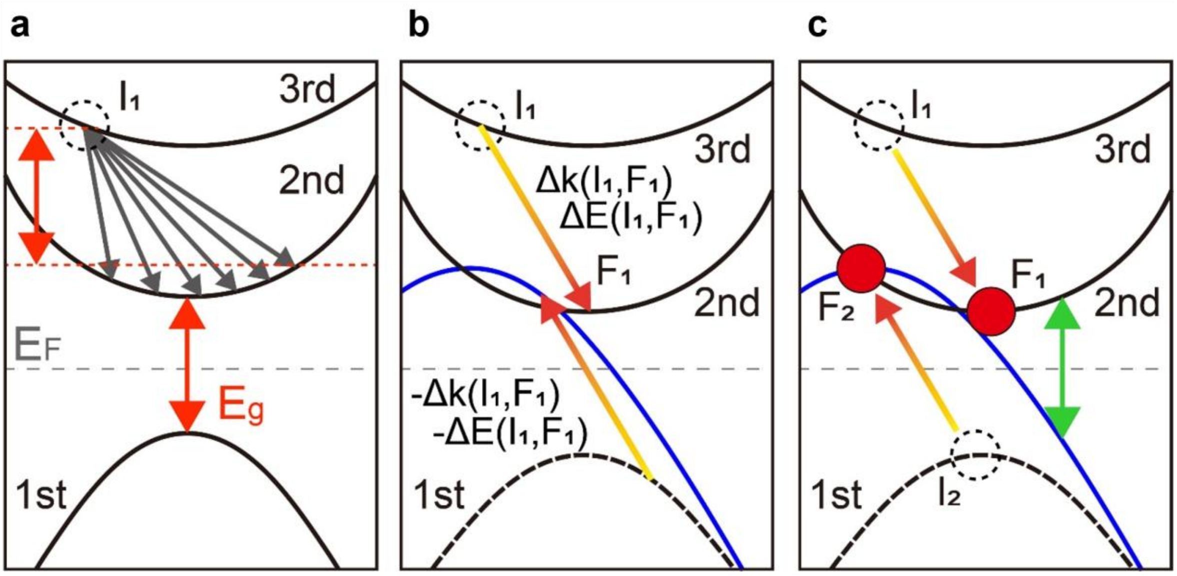

Figure S15. Schematic illustration of the generalized Bang-Kang approach. (**a**) Tested channels to transfer energy-momentum from the first carrier to the second. The gray arrows represent energy-momentum vectors with initial state $\boldsymbol{I_1}$. The energy gap size is described by the red double arrows. We only tested energy-momentum vectors with energy larger than the energy gap, $\boldsymbol{E_g}$. The dashed empty circle indicates the position of the resultant hole. (**b**) For a given energy-momentum vector, we shift the valence band in the opposite direction of the energy-momentum vector shown in **a**, as depicted by the blue band. (**c**) CM intensity can be efficiently evaluated by counting the density of the crossing states between the (blue) shifted valence and the (black) conduction bands. The green double arrow indicates the direct gap. Red solid circles indicate the positions of the multiplied electrons.

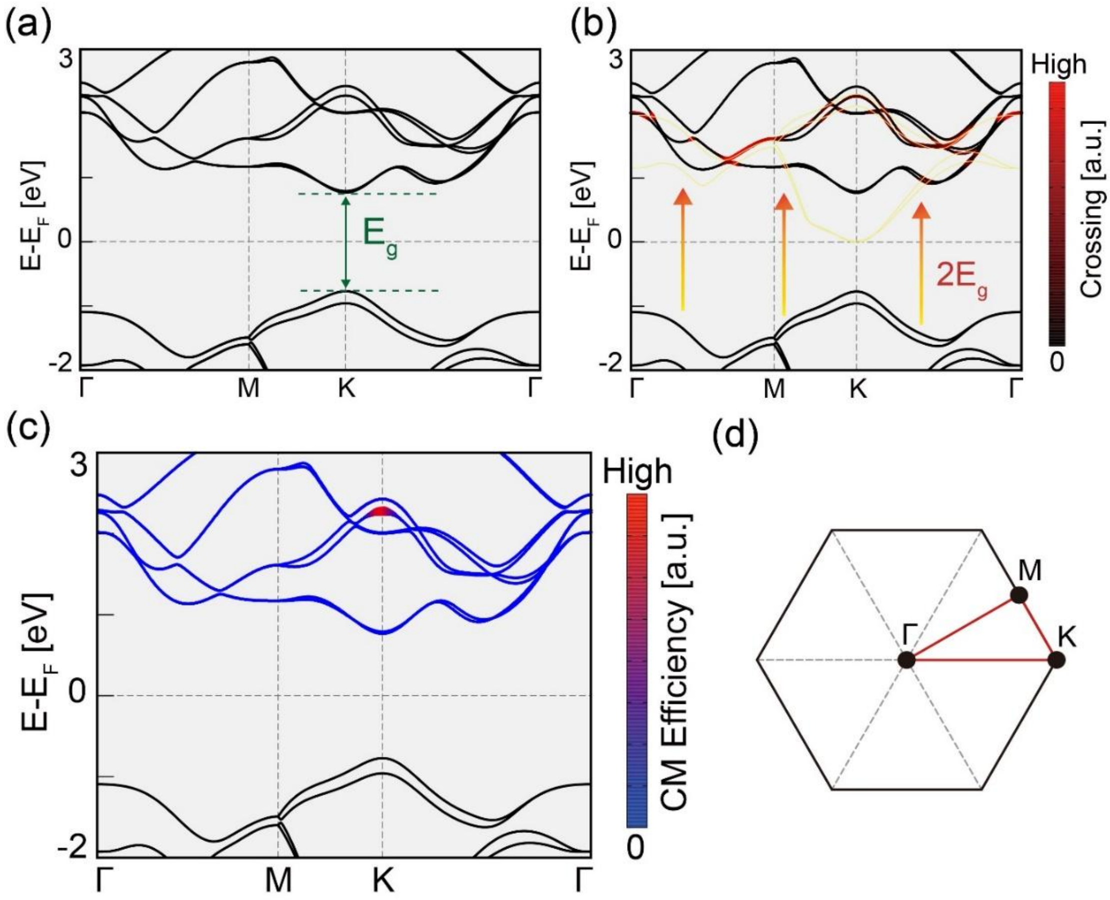

Figure S16. CM calculations for monolayer MoSe$_2$ at $2E_g$ excitation. (**a**) Band structure of monolayer MoSe$_2$ along the high-symmetry lines of the Brillouin zone (BZ) shown in (**d**). The direct band-gap $\boldsymbol{E_g}$ at $\boldsymbol{K}$ is highlighted by a green double arrow. (**b**) Crossing points between the $\boldsymbol{2E_g}$ shited valence bands (yellow) and the conduction bands. The intensity is contributed by function $\boldsymbol{\delta(\hbar\omega - E_{n_{I_1}}(k_{I_1}) + E_m(k_{I_1}))}$, which models a Gaussian function with a FWHM of 79.5 meV. The magnitude of $\boldsymbol{2E_g}$ is shown by orange arrows. (**c**) Calculated CM efficiency for the monolayer bands. The thickness of the lines scales with the contribution of CM. (**d**) The BZ, with high-symmetry lines highlighted red.

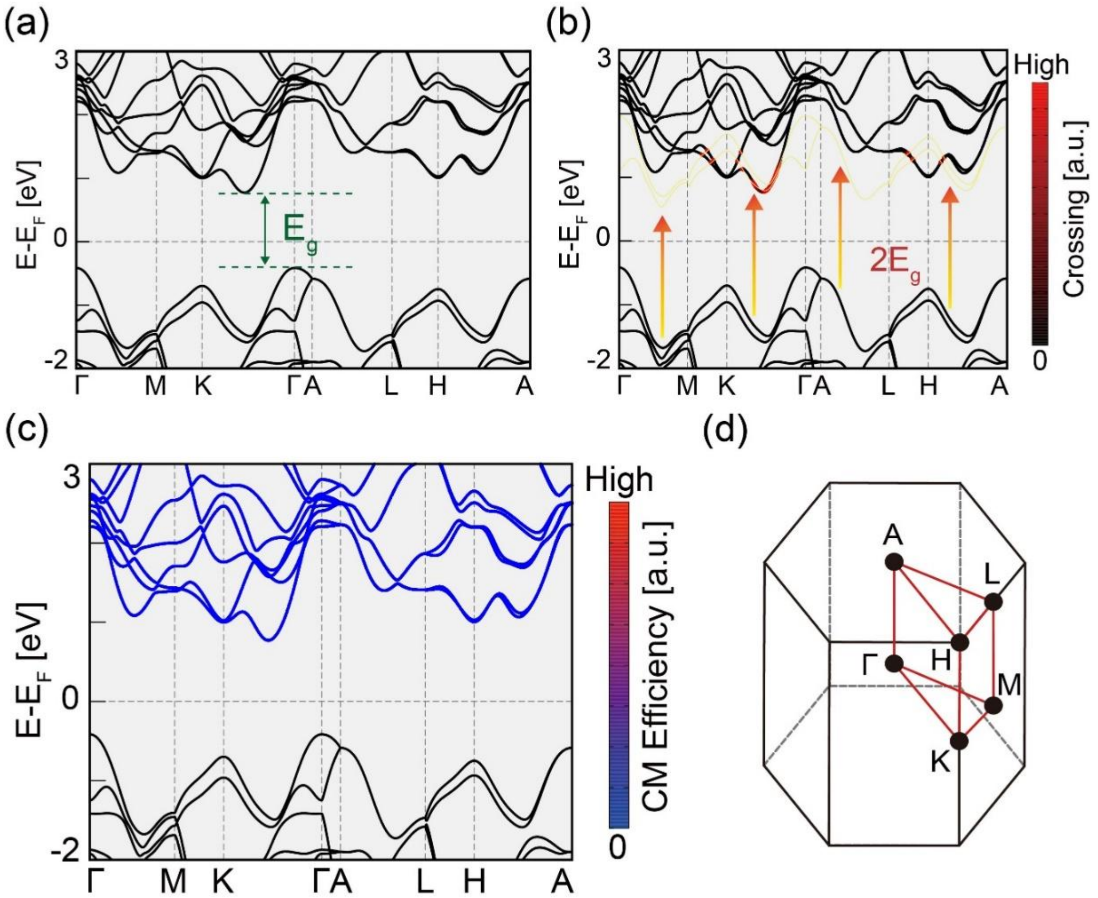

Figure S17. CM calculations for bulk MoSe₂ at $2E_g$ excitation. (a) Band structure of bulk MoSe₂ along the high-symmetry line of the hexagonal BZ shown in **(d)**. The indirect band gap $\boldsymbol{E_g}$ in the $\boldsymbol{K-\Gamma}$ line is indicated by a green double arrow. **(b)** Crossing points between the $\boldsymbol{2E_g}$ shifted valence bands (yellow) and the conduction bands. The intensity is contributed from the function $\boldsymbol{\delta(\hbar\omega - E_{n_{I_1}}(k_{I_1}) + E_m(k_{I_1}))}$, which models a Gaussian function with the FWHM of 50.6 meV. The size of $\boldsymbol{2E_g}$ is highlighted by orange arrows. **(c)** Calculated CM efficiency for the bluk bands along the high-symmetry lines. The thickness of lines scales with the contribution of CM. **(d)** BZ with the high-symmetry lines colored red.

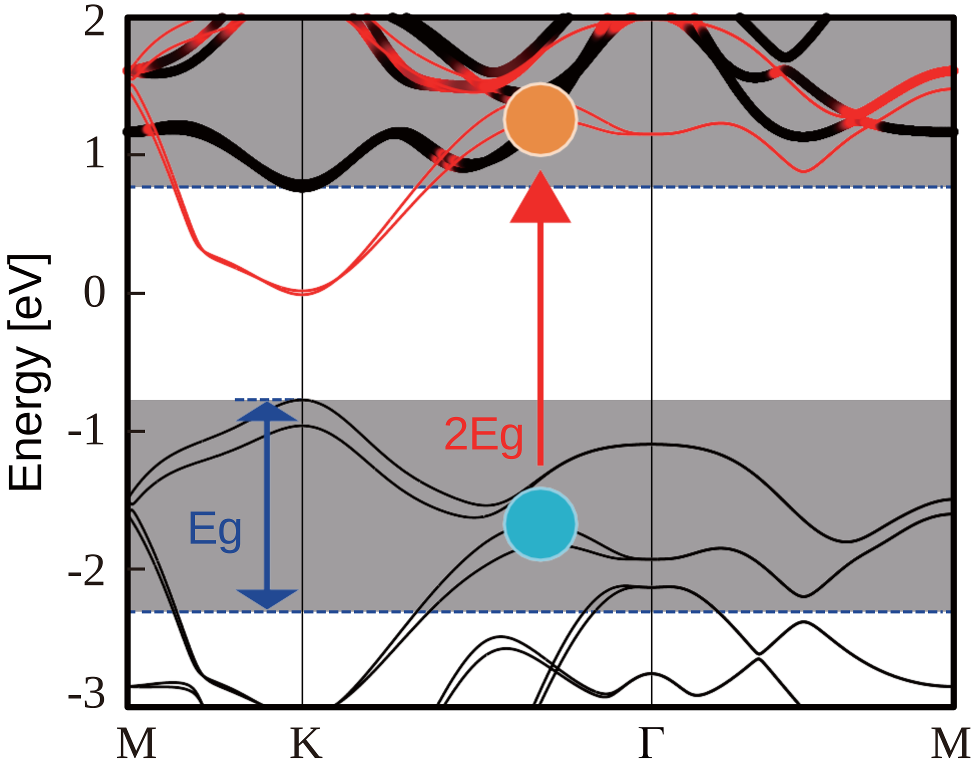

Figure S18. Creation of hole in valance bands by $2E_g$ excitation of electrons. The exemplary hole and electron are marked with blue and orange circles, respectively. The pristine band structure is shown with the black lines, while the red lines depict the energy-shifted valence bands. Possible excitation channels are colored in red on the conduction bands. The gray-shaded region corresponds to the ’forbidden zone’, where a valance band hole cannot contribute to the ideal CM process.

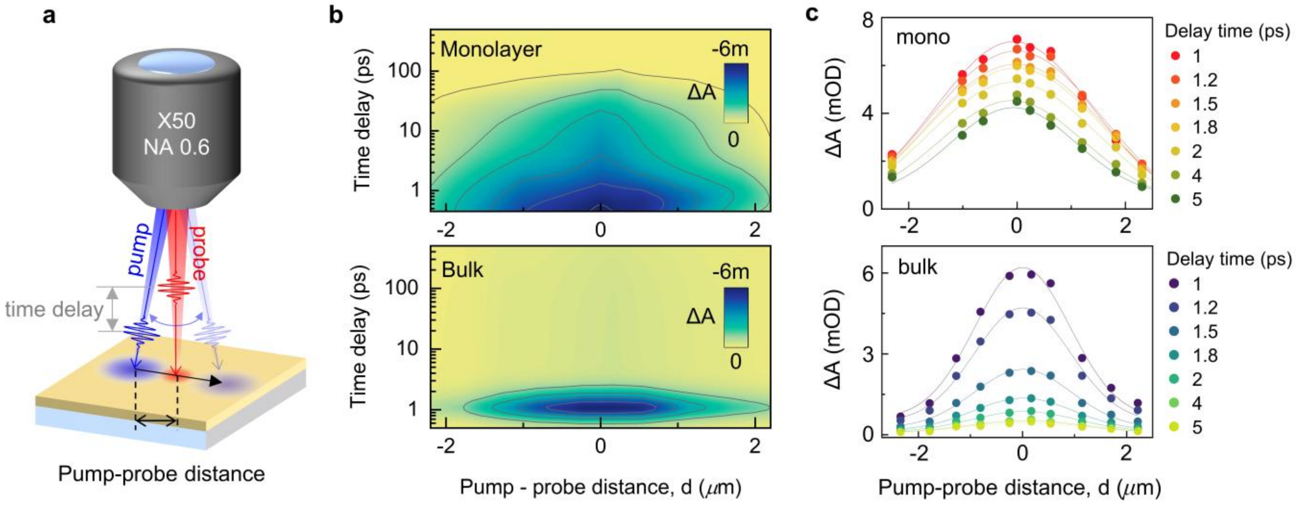

Figure S19. (**a**) Schematic of femtosecond spatiotemporal transient absorption microscopy (TAM). The probe is positioned at the center of the sample and scans transient absorption as a function of pump-probe distance and delay. (**b**) Spatial carrier distribution of monolayer (top) and bulk $MoSe_2$ (bottom) visualized by TAM. The carrier diffusion dynamics are represented through pseudo-color maps. (**c**) Pump-probe distance profiles of transient absorption (ΔA) for the monolayer (top) and bulk (bottom) at various time delays. Gaussian fitting of the spatial profiles (solid lines) was performed across the entire time delay range to extract detailed diffusion behavior over time (see **Note 7** in the **Supporting Information**).

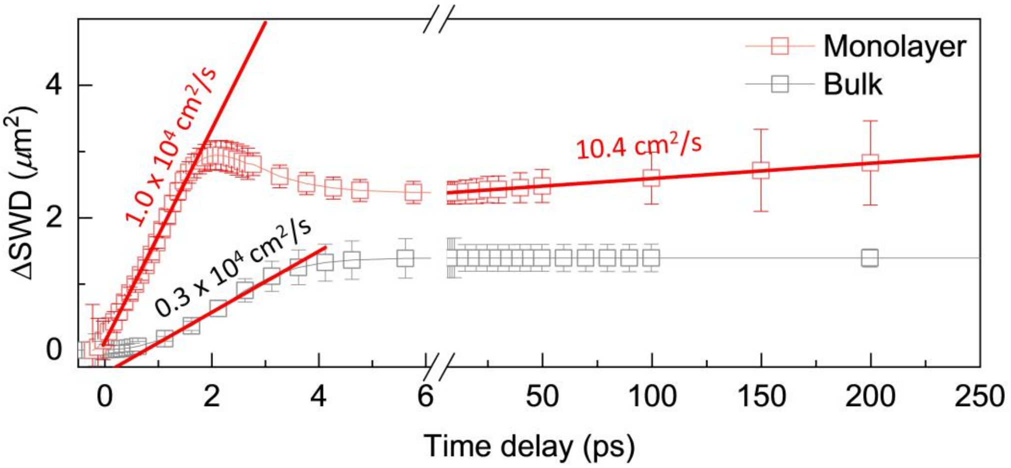

Figure S20. **Diffusion coefficient comparison between monolayer and bulk MoSe$_2$.** The temporal evolution of the squared width broadening (ΔSWD) was monitored for both the monolayer (red) and bulk (black). The diffusion coefficients were determined by performing linear fits (solid lines) to the data in the corresponding time regimes.

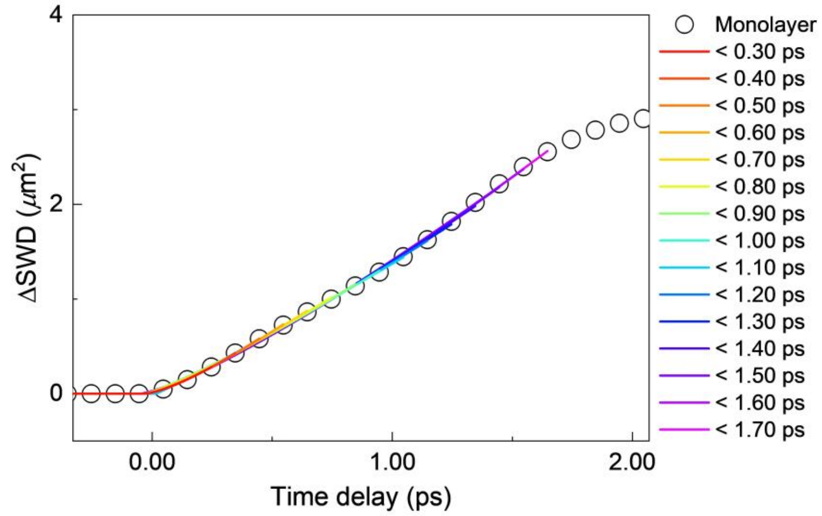

Figure S21. Evaluation of ballistic transport in monolayer $MoSe_2$. The temporal evolution of the square width distribution (SWD) in the monolayer is represented by open circles. To assess ballistic transport, the data was fitted using a power function with a transport exponent. This fitting was conducted meticulously at each time delay, starting from negative delay times. The obtained transport exponent as function of time delay as well as fitting error are presented in **Figure 3c**.

Table S2. Monolayer $MoSe_2$ absorbed photon density (APD) calculation

Energy (eV)	Wavelength (nm)	Before pinhole (nJ)	After pinhole (nJ)	Absorption	APD (*photons* / cm^2 / nJ)
3.54	350	22.2	2.25	0.13	5.23×10^{11}
3.26	380	100	20.00	0.11	9.81×10^{11}
3.18	390	150	25.00	0.11	8.40×10^{11}
3.10	400	60	17.50	0.11	1.50×10^{12}
3.18	410	27	2.50	0.11	4.65×10^{11}
2.48	500	36	20.00	0.12	3.91×10^{12}
2.25	550	23	8.70	0.08	1.84×10^{12}
2.07	600	128	18.00	0.05	4.93×10^{11}

Table S3. Bulk $MoSe_2$ APD calculation

Energy (eV)	Wavelength (nm)	Before pinhole (nJ)	After pinhole (nJ)	Absorption	APD (*photons* / cm^2 / nJ)
3.54	350	100	15.00	0.49	2.92×10^{12}
3.35	370	102	21.10	0.48	4.17×10^{12}
3.06	405	100	25.00	0.52	5.96×10^{12}
2.76	450	105	11.00	0.52	2.78×10^{12}
2.64	470	103	10.45	0.51	2.78×10^{12}
2.58	480	103	14.72	0.51	3.99×10^{12}
2.53	490	102	22.00	0.51	6.17×10^{12}
2.48	500	102	10.40	0.50	2.91×10^{12}
2.43	510	104	9.60	0.49	2.61×10^{12}
2.38	520	101	13.10	0.47	3.62×10^{12}
2.25	550	100	9.50	0.42	2.48×10^{12}
2.07	600	100	6.40	0.34	1.47×10^{12}
1.97	630	100	7.40	0.30	1.57×10^{12}

Table S4. CM conversion efficiency

	Material	CM efficiency (%)	Ref
0D	PbS	44	34
	PbS	40	35
	PbSe (4.7 nm)	41	36
	PbSe	3.12, 7.49, 19.76, 28.29, 37.38, 35.75, 31.85, 34.90	37
	PbSe	40	38, 39
	InP	30	40
	InAs	35	41
	Si (6.5 nm)	63	42
	Si	99	43
	Porous Si	96	43
	$FAPb_{0.93}Sn_{0.07}I_3$	87	44
	$FAPb_{0.96}Sn_{0.04}I_3$	73	44
	$FAPb_{0.89}Sn_{0.11}I_3$	64	44
	$FAPbI_3$	40	44
	$CsPbI_3$	98	45
1D	Si NR	61	42
	PbSe NR	80	46
	PbSe NR	70	47
	PbSe NR	75	36
2D	$MoTe_2$	99	48
	PbS NS (4 nm)	90	49
	PbS NS (5.9 nm)	50	49
	PbS NS (7 nm)	55	49
	BP (2L)	93	28
	BP (3L)	79	28
	BP (4L)	71	28
3D	PbS	29	50
	PbSe	19	50
	Ge	40	51
	Ge	45	52
	Si	57	51
	Si	57	52

where NR indicates nanorod and NS is nanosheet.

References

1. M. Selig, G. Berghäuser, M. Richter, R. Bratschitsch, A. Knorr and E. Malic, *2d Materials*, 2018, **5**, 035017.
2. P. Valencia-Acuna, P. Zereshki, M. M. Tavakoli, J. H. Park, J. Kong and H. Zhao, *Phys. Rev. B*, 2020, **102**, 035414.
3. F. Ceballos, Q. N. Cui, M. Z. Bellus and H. Zhao, *Nanoscale*, 2016, **8**, 11681-11688.
4. P. Steinleitner, P. Merkl, P. Nagler, J. Mornhinweg, C. Schüller, T. Korn, A. Chernikov and R. Huber, *Nano Lett.*, 2017, **17**, 1455-1460.
5. E. J. Sie, A. Steinhoff, C. Gies, C. H. Luo, Q. Ma, M. Rösner, G. Schönhoff, F. Jahnke, T. O. Wehling, Y. H. Lee, J. Kong, P. Jarillo-Herrero and N. Gedik, *Nano Lett.*, 2017, **17**, 4210-4216.
6. J. H. Kim, M. R. Bergren, J. C. Park, S. Adhikari, M. Lorke, T. Frauenheim, D. H. Choe, B. Kim, H. Choi, T. Gregorkiewicz and Y. H. Lee, *Nat. Commun.*, 2019, **10**.
7. G. Kaur, K. J. Babu and H. N. Ghosh, *J. Phys. Chem. Lett.*, 2020, **11**, 6206-6213.
8. Q. Liu, K. Wei, Y. Tang, Z. Xu, X. Cheng and T. Jiang, *Adv. Sci.*, 2022, **9**, e2105746.
9. T. Wang, T. R. Hopper, N. Mondal, S. H. Liu, C. N. Yao, X. J. Zheng, F. Torrisi and A. A. Bakulin, *Acs Nano*, 2023, **17**, 6330-6340.
10. M. C. Beard, A. G. Midgett, M. C. Hanna, J. M. Luther, B. K. Hughes and A. J. Nozik, *Nano Lett.*, 2010, **10**, 3019-3027.
11. W. Zheng, M. Bonn and H. I. Wang, *Nano Lett.*, 2020, **20**, 5807-5813.
12. J. Bang and J. Kang, *Phys. Rev. B*, 2021, **104**, 035417.
13. R. Rosati, R. Perea-Causin, S. Brem and E. Malic, *Nanoscale*, 2020, **12**, 356-363.
14. N. Kumar, Q. Cui, F. Ceballos, D. He, Y. Wang and H. Zhao, *Nanoscale*, 2014, **6**, 4915-4919.
15. M. Seitz, A. J. Magdaleno, N. Alcazar-Cano, M. Melendez, T. J. Lubbers, S. W. Walraven, S. Pakdel, E. Prada, R. Delgado-Buscalioni and F. Prins, *Nat. Commun.*, 2020, **11**, 2035.
16. S. Pan, W. Kong, J. Liu, X. Ge, P. Zereshki, S. Hao, D. He, Y. Wang and H. Zhao, *ACS Appl. Nano Mater.*, 2018, **2**, 459-464.
17. M.-L. Tsai, S.-H. Su, J.-K. Chang, D.-S. Tsai, C.-H. Chen, C.-I. Wu, L.-J. Li, L.-J. Chen and J.-H. He, *ACS Nano*, 2014, **8**, 8317-8322.
18. K. Nassiri Nazif, A. Daus, J. Hong, N. Lee, S. Vaziri, A. Kumar, F. Nitta, M. E. Chen, S. Kananian, R. Islam, K.-H. Kim, J.-H. Park, A. S. Y. Poon, M. L. Brongersma, E. Pop and K. C. Saraswat, *Nat. Commun.*, 2021, **12**, 7034.
19. D. Moon, W. Lee, C. Lim, J. Kim, J. Kim, Y. Jung, H. Y. Choi, W. S. Choi, H. Kim, J. H. Baek,

C. Kim, J. Joo, H. G. Oh, H. Jang, K. Watanabe, T. Taniguchi, S. Bae, J. Son, H. Ryu, J. Kwon, H. Cheong, J. W. Han, H. Jang and G. H. Lee, *Nature*, 2025, **638**, 957–964.

20. L. Li, Q. Q. Wang, F. F. Wu, Q. L. Xu, J. P. Tian, Z. H. Huang, Q. H. Wang, X. Zhao, Q. H. Zhang, Q. K. Fan, X. Z. Li, Y. L. Peng, Y. K. Zhang, K. S. Ji, A. M. Zhi, H. C. Sun, M. T. Zhu, J. D. Zhu, N. P. Lu, Y. Lu, S. P. Wang, X. D. Bai, Y. Xu, W. Yang, N. Li, D. X. Shi, L. D. Xian, K. H. Liu, L. J. Du and G. Y. Zhang, *Nat. Commun.*, 2024, **15**, 1825
21. T. F. Yang, B. Y. Zheng, Z. Wang, T. Xu, C. Pan, J. Zou, X. H. Zhang, Z. Y. Qi, H. J. Liu, Y. X. Feng, W. D. Hu, F. Miao, L. T. Sun, X. F. Duan and A. L. Pan, *Nat. Commun.*, 2017, **8**, 1906.
22. T. Kang, T. W. Tang, B. J. Pan, H. W. Liu, K. N. Zhang and Z. T. Luo, *ACS Mater. Au*, 2022, **2**, 665-685.
23. S. Seo, S. Kim, H. Choi, J. Lee, H. Yoon, G. Piao, J. C. Park, Y. Jung, J. Song, S. Y. Jeong, H. Park and S. Lee, *Adv. Sci.*, 2019, **6**, 1900301.
24. X. Duan, C. Wang, J. C. Shaw, R. Cheng, Y. Chen, H. Li, X. Wu, Y. Tang, Q. Zhang, A. Pan, J. Jiang, R. Yu, Y. Huang and X. Duan, *Nat. Nanotechnol.*, 2014, **9**, 1024-1030.
25. S. Pace, L. Martini, D. Convertino, D. H. Keum, S. Forti, S. Pezzini, F. Fabbri, V. Miseikis and C. Coletti, *ACS Nano*, 2021, **15**, 4213-4225.
26. S. Ahn, G. Kim, P. K. Nayak, S. I. Yoon, H. Lim, H. J. Shin and H. S. Shin, *ACS Nano*, 2016, **10**, 8973-8979.
27. H. U. Kim, V. Kanade, M. Kim, K. S. Kim, B. S. An, H. Seok, H. Yoo, L. E. Chaney, S. I. Kim, C. W. Yang, G. Y. Yeom, D. Whang, J. H. Lee and T. Kim, *Small*, 2020, **16**, 1905000.
28. Q. Zhou, H. Zhou, W. Tao, Y. Zheng, Y. Chen and H. Zhu, *Nano Lett.*, 2020, **20**, 8212-8219.
29. Y. J. Sun, D. Wang and Z. G. Shuai, *J. Phys. Chem. C*, 2016, **120**, 21866-21870.
30. S. K. Pandey, R. Das and P. Mahadevan, *Acs Omega*, 2020, **5**, 15169-15176.
31. J. Quereda, T. S. Ghiasi, J. S. You, J. van den Brink, B. J. van Wees and C. H. van der Wal, *Nat. Commun.*, 2018, **9**, 3346.
32. D. Nam, J. U. Lee and H. Cheong, *Sci. Rep.*, 2015, **5**, 17113.
33. P. Tonndorf, R. Schmidt, P. Bottger, X. Zhang, J. Borner, A. Liebig, M. Albrecht, C. Kloc, O. Gordan, D. R. T. Zahn, S. M. de Vasconcellos and R. Bratschitsch, *Opt. Express*, 2013, **21**, 4908-4916.
34. A. G. Midgett, J. M. Luther, J. T. Stewart, D. K. Smith, L. A. Padilha, V. I. Klimov, A. J. Nozik and M. C. Beard, *Nano Lett.*, 2013, **13**, 3078-3085.
35. S. J. O. Hardman, D. M. Graham, S. K. Stubbs, B. F. Spencer, E. A. Seddon, H. T. Fung, S.

Gardonio, F. Sirotti, M. G. Silly, J. Akhtar, P. O'Brien, D. J. Binks and W. R. Flavell, *Phys. Chem. Chem. Phys.*, 2011, **13**, 20275-20283.

36. P. D. Cunningham, J. E. Boercker, E. E. Foos, M. P. Lumb, A. R. Smith, J. G. Tischler and J. S. Melinger, *Nano Lett.*, 2011, **11**, 3476-3481.
37. C. S. Sandeep, S. ten Cate, J. M. Schins, T. J. Savenije, Y. Liu, M. Law, S. Kinge, A. J. Houtepen and L. D. Siebbeles, *Nat. Commun.*, 2013, **4**, 2360.
38. J. A. McGuire, M. Sykora, J. Joo, J. M. Pietryga and V. I. Klimov, *Nano Lett.*, 2010, **10**, 2049-2057.
39. A. G. Midgett, H. W. Hillhouse, B. K. Hughes, A. J. Nozik and M. C. Beard, *J. Phys. Chem. C*, 2010, **114**, 17486-17500.
40. S. K. Stubbs, S. J. O. Hardman, D. M. Graham, B. F. Spencer, W. R. Flavell, P. Glarvey, O. Masala, N. L. Pickett and D. J. Binks, *Phys. Rev. B*, 2010, **81**, 081303.
41. R. D. Schaller, J. M. Pietryga and V. I. Klimov, *Nano Lett.*, 2007, **7**, 3469-3476.
42. C. J. Stolle, X. Lu, Y. Yu, R. D. Schaller and B. A. Korgel, *Nano Lett.*, 2017, **17**, 5580-5586.
43. D. Timmerman, J. Valenta, K. Dohnalova, W. D. A. M. de Boer and T. Gregorkiewicz, *Nat. Nanotechnol.*, 2011, **6**, 710-713.
44. Y. F. Chen, J. Yin, Q. Wei, C. H. Wang, X. T. Wang, H. Ren, S. F. Yu, O. M. Bakr, O. F. Mohammed and M. J. Li, *Nat. Photonics*, 2022, **16**, 485-490.
45. C. de Weerd, L. Gomez, A. Capretti, D. M. Lebrun, E. Matsubara, J. H. Lin, M. Ashida, F. C. M. Spoor, L. D. A. Siebbeles, A. J. Houtepen, K. Suenaga, Y. Fujiwara and T. Gregorkiewicz, *Nat. Commun.*, 2018, **9**, 4199.
46. A. Kulkarni, W. H. Evers, S. Tomic, M. C. Beard, D. Vanmaekelbergh and L. D. A. Siebbeles, *ACS Nano*, 2018, **12**, 378-384.
47. R. L. Sandberg, L. A. Padilha, M. M. Qazilbash, W. K. Bae, R. D. Schaller, J. M. Pietryga, M. J. Stevens, B. Baek, S. W. Nam and V. I. Klimov, *ACS Nano*, 2012, **6**, 9532-9540.
48. J. H. Kim, M. R. Bergren, J. C. Park, S. Adhikari, M. Lorke, T. Frauenheim, D. H. Choe, B. Kim, H. Choi, T. Gregorkiewicz and Y. H. Lee, *Nat. Commun.*, 2019, **10**, 5488.
49. M. Aerts, T. Bielewicz, C. Klinke, F. C. Grozema, A. J. Houtepen, J. M. Schins and L. D. Siebbeles, *Nat. Commun.*, 2014, **5**, 3789.
50. J. J. H. Pijpers, R. Ulbricht, K. J. Tielrooij, A. Osherov, Y. Golan, C. Delerue, G. Allan and M. Bonn, *Nat. Phys.*, 2009, **5**, 811-814.
51. M. Wolf, R. Brendel, J. H. Werner and H. J. Queisser, *J. Appl. Phys.*, 1998, **83**, 4213-4221.

52. O. Christensen, *J. Appl. Phys.*, 1976, **47**, 689-695.